crystals

MDPI

Article

Preliminary Study on the Heterogeneous Nucleation Behavior and Interfacial Mechanism of Lysozyme Regulated by Silica Nanoparticles

Qihang Chen, Xiujian Cui and Xiangyang Zhang *

State Key Laboratory of Chemical Engineering, East China University of Science and Technology, Shanghai 200237, China; y82230011@mail.ecust.edu.cn (Q.C.); cxj313905@163.com (X.C.)
* Correspondence: zxydcom@ecust.edu.cn

Abstract

Protein crystal nucleation remains difficult to predict and control and is still a critical issue in structural biology, protein crystal formulations, and crystal engineering. Heterogeneous nucleants can regulate protein crystallization by providing solid interfaces, enriching protein molecules, and stabilizing prenucleation aggregates; however, their dominant action stage, particle-size effect, and interfacial interaction mechanism remain unclear. In this study, hen egg white lysozyme (HEWL) was selected as a model protein, and silica nanoparticles (SNPs) with average diameters of 80, 120, and 200 nm were prepared using the modified Stöber method. Under a constant total particle surface area, the effects of SNPs on HEWL crystallization, prenucleation aggregation, interfacial adsorption, and subsequent crystal growth were systematically investigated. The results showed that, under 30 mg·mL^{-1} HEWL and 0.6 M NaCl conditions, all SNPs shortened the apparent induction time, with 200 nm SNPs showing the strongest effect. In contrast, 80 nm SNPs produced the largest crystal size at the fixed observation time of 72 h, suggesting that crystal size within a fixed incubation period is jointly affected by nucleation rate, nucleus number, local solute consumption, and subsequent crystal growth. Under low protein concentration and low NaCl concentration conditions, SNPs promoted crystal formation in systems with weak spontaneous nucleation. Zeta potential, UV-Vis, fluorescence, FT-IR, CD, and DLS results suggested that SNPs interacted with HEWL at the interface and promoted apparent aggregation behavior, whereas polarized optical microscopy indicated no detectable influence on the later linear growth of visible crystals. These results suggest that SNPs mainly affect processes before visible crystal formation and provide insight into their application as heterogeneous nucleants for protein crystallization.

Keywords: silica nanoparticles; lysozyme; heterogeneous nucleation; protein crystallization; interfacial adsorption; molecular simulation

Received: 2 June 2026
Revised: 3 July 2026
Accepted: 5 July 2026
Published: 9 July 2026

1. Introduction

Protein crystallization is not only an essential prerequisite for single-crystal X-ray diffraction structure determination [1], but it also has broad applications in protein crystal formulations [2], protein purification and separation [3], and crystal engineering [4]. In recent years, although cryo-electron microscopy (cryo-EM) [5] and structural prediction methods such as AlphaFold [6] have significantly expanded the scope of structural biology, high-quality protein crystals remain indispensable for high-resolution structural determination [7], ligand-complex analysis [8], crystal drug delivery [9], and crystallization process

engineering [10]. For many protein systems, obtaining crystals with controllable nucleation density, large size, and regular morphology while avoiding amorphous precipitation and burst nucleation remains a major challenge in crystallization experiments [11].

Nucleation [11] is the most stochastic and difficult stage to control during protein crystallization. Classical nucleation theory [12] emphasizes that nucleus formation must overcome the nucleation barrier associated with solid–liquid interfacial free energy, whereas the two-step nucleation theory [13] proposes that protein-rich dense liquid droplets or prenucleation aggregates may form before the appearance of stable nuclei. Therefore, promoting local protein enrichment, stabilizing prenucleation intermediates, and reducing the nucleation barrier under low-supersaturation conditions are expected to improve crystallization success and optimize crystal size distribution. Heterogeneous nucleants [14] were developed based on these physicochemical principles. According to heterogeneous nucleation theory [15], the major role of solid interfaces is not to directly accelerate all crystal growth processes, but rather to increase the probability of critical nucleus formation by reducing effective interfacial free energy, altering contact angles, or increasing local protein concentration near the interface.

Naomi Chayen and co-workers systematically proposed the use of silicon-based porous materials for protein crystallization [16] and demonstrated that porous silicon could promote crystal formation for various proteins under conditions insufficient for spontaneous nucleation. Subsequently, the concept of a "universal nucleant" and its nucleation mechanisms in porous materials were further developed [14], emphasizing the critical roles of pore size, surface properties, and interfacial geometry in protein nucleation. Previous studies [17,18] suggested that pore confinement, wall stabilization, pore-size matching, and interfacial stabilization synergistically reduce the nucleation barrier. In addition, studies based on mesoporous silica templates such as SBA-15 [19] demonstrated that pre-saturation adsorption of target proteins on the template could alleviate the rapid depletion of protein concentration in the bulk solution, thereby expanding the metastable region and improving heterogeneous crystallization efficiency. However, the mechanisms involving pore confinement and two-dimensional nucleus stabilization in porous materials cannot fully explain the action pathway of nonporous spherical nanoparticles.

SNPs [20] possess tunable particle size, abundant surface silanol groups, high chemical stability, and good biocompatibility. In typical weakly acidic crystallization buffers such as sodium acetate buffer (pH 4.6), SNPs exhibit negatively charged surfaces, whereas hen egg white lysozyme (HEWL), with an isoelectric point of approximately 10–11, carries an overall positive charge [21]. This complementary surface-charge profile provides a strong electrostatic adsorption basis between SNPs and HEWL, while surface silanol groups also provide potential hydrogen-bonding sites. Previous studies have preliminarily shown that the addition of SNPs can expand the crystallization window of lysozyme and shorten the induction time for crystal formation, while SNPs with different particle sizes exhibit significantly different regulatory effects [22]. However, how particle size systematically affects prenucleation aggregation kinetics, crystallization windows, and subsequent crystal growth remains unclear. In addition, whether SNPs mainly function during interfacial enrichment before nucleation or during later visible crystal growth still requires systematic clarification through multidimensional characterization and theoretical simulation.

Accordingly, this study employed nonporous spherical SNPs and HEWL as a model system to systematically investigate the influence of SNP particle-size effects on the key stages of protein crystallization and the associated interfacial interaction mechanisms. First, the structures and surface properties of three sizes of SNPs were characterized. Subsequently, their regulatory effects on HEWL crystallization behavior were evaluated under different protein concentrations and precipitant concentrations. Combined

with Zeta potential analysis, spectroscopic techniques, DLS measurements, and microscopic observations, mechanistic evidence involving "interfacial adsorption—prenucleation aggregation—subsequent crystal growth" was constructed from a physicochemical perspective. Finally, molecular docking and molecular dynamics simulations were performed to provide a preliminary molecular-level explanation for SNP-regulated protein nucleation.

2. Materials and Methods

2.1. Preparation and Characterization of SNPs

SNPs were prepared using the modified Stöber method [23], as shown in Equations (1) and (2). Different particle sizes were obtained by adjusting the ratios of tetraethyl orthosilicate, ammonia, ethanol, and water. The resulting particles were collected by centrifugation, washed, and dried prior to characterization and crystallization experiments. PXRD was used to analyze the crystallinity of the particles. FT-IR was employed to identify Si–O–Si, Si–OH, and adsorbed water vibrations on the particle surfaces. SEM was used to observe particle morphology and determine particle size distribution. Specific surface area was measured using the BET method [24]. In crystallization experiments, to maintain a constant geometric specific surface area, the actual addition mass of SNPs with different particle sizes was calculated according to the BET surface area [24,25], ensuring that the initial theoretical total surface area of SNPs in each crystallization solution remained constant at 1.0×10^{16} $nm^2 \cdot mL^{-1}$.

$$Si(OCH_2CH_5)_4 + 4H_2O \xrightarrow{NH_3 \cdot H_2O} Si(OH)_4 + 4C_2H_5OH \quad (1)$$

$$Si(OH)_4 + Si(OCH_2CH_5)_4 \xrightarrow{NH_3 \cdot H_2O} SiO_2 \downarrow + 4C_2H_5OH \quad (2)$$

2.2. Lysozyme Crystallization Experiments and Statistical Analysis

According to previous reports [26–35] (Table S1), HEWL solutions were prepared in 0.1 M sodium acetate buffer (pH 4.6), and NaCl was used as the precipitant. Crystallization experiments were performed using the hanging-drop vapor diffusion method at 20 °C. Preliminary screening experiments compared the effects of different NaCl concentrations and different sizes of SNPs on HEWL crystal formation (Table S2). Subsequently, 30 $mg \cdot mL^{-1}$ HEWL and 0.6 M NaCl were selected as the primary comparison system, under which the control group could still nucleate spontaneously and belonged to a relatively low supersaturation region [36]. Experiments included a particle-free control group and SNP-added groups containing 80, 120, and 200 nm SNPs, respectively. The total SNP surface area was maintained constant, and each group contained independent parallel experiments (n = 3). The crystallization state inside the droplets was observed every 30 min using polarized optical microscopy, and the apparent induction time was recorded. Nucleation time was defined as the induction time when the first protein crystal was observed within the central concentric circle range (radius $\leq$ 1500 μm) [37]. The ending time referred to the time when the average crystal size change remained below 5% for three consecutive observation points [38]. The maximum crystal size and crystal size distribution at the fixed incubation time of 72 h were further statistically analyzed. Additional experiments were conducted under lower protein concentration conditions (15 $mg \cdot mL^{-1}$ HEWL) and different NaCl concentrations (0.3–1.5 M) to evaluate the ability of SNPs to expand the nucleation window. The optimal addition range of 200 nm SNPs was also investigated.

2.3. Characterization of Interfacial Interactions and Aggregation Dynamics

Zeta potential analysis was performed to investigate the surface charge characteristics of SNPs and the electrostatic interaction basis between SNPs and HEWL. UV-Vis spectroscopy

was used to monitor changes in the characteristic absorption of aromatic residues near 280 nm. Fluorescence spectroscopy was used to analyze the quenching behavior of intrinsic HEWL fluorescence induced by SNPs. FT-IR spectroscopy focused on shifts in the amide I and amide II bands of HEWL. CD spectroscopy was used to evaluate changes in the secondary structure content of HEWL before and after adsorption. Considering that nanoparticles may introduce scattering backgrounds during spectral measurements, all spectroscopic data were subjected to baseline correction and interpreted comprehensively using multiple characterization methods.

DLS was employed to monitor the evolution of the hydrodynamic diameter (Rh-average) of protein complexes or aggregates during the early crystallization stage before visible crystal formation, thereby evaluating the apparent dynamics of prenucleation aggregation. To clarify subsequent crystal growth behavior, visible crystals were continuously observed under polarized optical microscopy, and the later linear growth rates of crystals in the presence and absence of SNPs were calculated and compared.

2.4. Molecular Simulation

Molecular docking was used to predict potential binding sites and major interaction types between SNP model clusters [39] and HEWL, including electrostatic interactions, hydrogen bonding, and hydrophobic interactions [40]. Subsequently, based on the optimal complex conformation obtained from docking, molecular dynamics simulations were performed to investigate the conformational perturbation mechanism of SNP interfacial adsorption on local flexible regions and secondary-structure microenvironments of HEWL. The simulation results were used to provide molecular-level mechanistic support for the experimental observations.

AutoDock 4.2.6 (The Scripps Research Institute, La Jolla, CA, USA) and Materials Studio (Version 2019, Accelrys Software Inc., San Diego, CA, USA) were used for molecular docking and molecular dynamics simulations related to HEWL crystallization. Detailed simulation information is provided in the Supporting Information.

3. Results and Discussion

3.1. Structural and Surface Properties of SNPs

PXRD results (Figure 1A) showed that all three SNPs exhibited a typical broad amorphous silica diffraction halo near $2\theta \approx 22^{\circ}$, without sharp crystalline diffraction peaks. In the FT-IR spectra (Figure 1B), the absorption bands at 3000–3500 cm^{-1} and 1633 cm^{-1} were assigned to the O–H stretching vibration and bending vibration of adsorbed water, respectively. Characteristic peaks at 467, 561, 803, 957, and 1100 cm^{-1} corresponded to vibrations associated with Si–O, Si–OH, O–Si–O, and Si–O–Si groups. The FT-IR spectra of the three particle sizes were highly similar, indicating consistent surface chemical compositions. SEM images (Figure 1C) confirmed that all SNPs exhibited regular near-spherical morphology with monodisperse particle-size distributions. The average particle sizes were 80.5 ± 0.7 nm, 120.3 ± 0.6 nm, and 202.7 ± 3.6 nm, respectively. BET nitrogen adsorption analysis (Figure 1D) showed that the specific surface areas of the 80, 120, and 200 nm SNPs were 77, 39, and 33 $m^2 \cdot g^{-1}$, respectively. These results confirmed the successful preparation of spherical amorphous silica nanoparticles with significant particle-size gradients while maintaining highly similar structural and surface chemical characteristics.

3.2. Size-Dependent Effects of SNPs on HEWL Crystallization Kinetics

To minimize interference from rapid spontaneous nucleation or amorphous precipitation under highly supersaturated conditions, while maintaining measurable induction time and crystal-size data for the particle-free control group within the experimental observation window, 30 $mg \cdot mL^{-1}$ HEWL and 0.6 M NaCl were selected as the representative crystallization system for comparing SNP particle-size effects. Under these conditions, the addition

of SNPs with different particle sizes significantly altered crystallization kinetics (Figure 2). To reduce the influence of observation time differences on crystal-size comparison and ensure that measurable crystals appeared in all groups after 24 h, 72 h was selected as the fixed observation point according to the maximum induction time among all experimental groups. At 72 h, crystal sizes in all SNP-containing groups were generally larger than those in the particle-free control group (Figure 2A). The induction time of the control group was 803 ± 30 min, whereas the induction times decreased significantly to 482 ± 18, 467 ± 17, and 400 ± 20 min after adding 80, 120, and 200 nm SNPs, respectively (Figure 2B). The maximum crystal size in the 80 nm SNP group reached approximately 173 μm, which was larger than that of the control group (~94 μm), whereas the maximum crystal sizes in the 120 and 200 nm SNP groups were approximately 136 and 116 μm, respectively (Figure 2C).

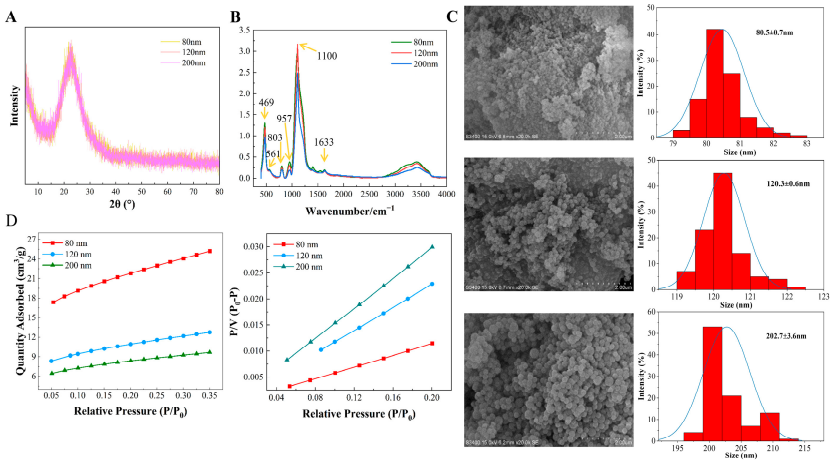

Figure 1. Structural characteristics and surface properties of SNPs. (**A**) PXRD patterns; (**B**) FT-IR spectra; (**C**) SEM images of SNPs with three different particle sizes and the corresponding particle-size distribution histograms. The blue curves indicate Gaussian fits to the particle-size distributions; (**D**) BET nitrogen adsorption–desorption isotherms (**left**) and linear fitting curves for specific surface area analysis (**right**).

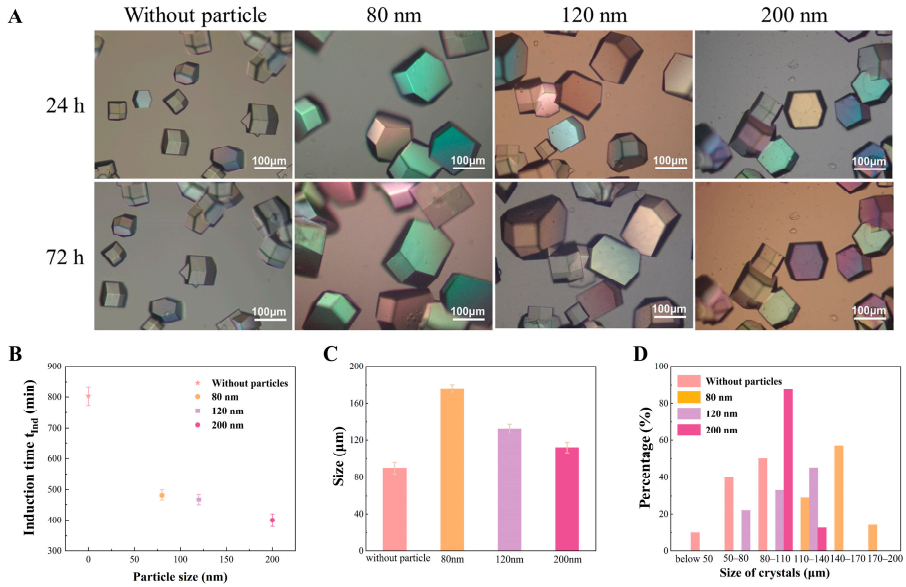

Figure 2. Effects of SNPs with different particle sizes on the crystallization behavior of HEWL (30 mg·mL^{-1} HEWL, 0.6 M NaCl). (**A**) Optical microscopic images of HEWL crystals. The colors observed in the optical micrographs result from optical imaging effects and have no specific scientific meaning. (**B**) Comparison of crystallization induction times. (**C**) Comparison of crystal sizes at 72 h. (**D**) Crystal size distributions at 72 h.

Based on heterogeneous nucleation theory, the decrease in induction time with increasing SNP size suggests that larger nanoparticles may provide more favorable interfacial environments for local enrichment of HEWL and early nucleation events at the solid–liquid interface [41].

Notably, although 200 nm SNPs exhibited the shortest induction time, 80 nm SNPs produced the largest crystal size within 72 h. Combined with the crystal size distribution results (Figure 2D), the nucleation-promoting effect of SNPs may not exhibit a simple positive correlation with crystal size within a fixed observation period. A possible explanation is that larger SNPs may trigger earlier nucleation events. If more nuclei are formed within the droplet, local supersaturation would be consumed more rapidly, limiting the subsequent growth of individual crystals. In contrast, 80 nm SNPs may induce a relatively moderate nucleation process, allowing some crystals to access sufficient solute supply and growth space during subsequent incubation [36]. However, the present observations do not allow a direct quantitative relationship among induction time, nucleus number, and crystal size to be established. Therefore, this interpretation should be regarded as a plausible mechanistic explanation rather than a definitive conclusion. Future quantitative studies would be valuable to further evaluate this relationship.

3.3. Evaluation of SNPs for Expanding the Low-Supersaturation Nucleation Window

To further evaluate the nucleation-inducing ability of SNPs under conditions with insufficient spontaneous nucleation, the HEWL concentration was reduced from 30 mg·mL^{-1} in the primary crystallization system to 15 mg·mL^{-1}, and HEWL crystallization behavior in the presence of SNPs with different particle sizes was investigated under low-protein-concentration conditions (Figure 3A). This concentration is lower than the commonly used concentration range in many HEWL crystallization screening studies [42]. Under the observation window used in this study, no visible crystals were observed in the particle-free control group, indicating spontaneous nucleation was kinetically frustrated under these conditions. In contrast, crystal formation was observed in all SNP-containing systems, with 200 nm SNPs showing the most pronounced nucleation-promoting effect.

At the original protein concentration (30 mg·mL^{-1} HEWL), different concentrations of 200 nm SNPs were added to investigate the influence of nanoparticle concentration on crystallization behavior (Figure 3B). Moderate SNP dosage promoted crystallization, whereas excessive dosage induced precipitation or uncontrolled nucleation. When the SNP concentration reached 1.0 mg·mL^{-1}, crystals and amorphous precipitates coexisted.

Precipitant concentration gradient experiments further showed that, in the 0.5 M NaCl system, SNPs shortened the nucleation time from several days to within 24 h. Under the even lower 0.3 M NaCl condition, only the 120 and 200 nm SNPs successfully induced crystallization (Figure 3C), confirming that larger nanoparticles could establish local microenvironments satisfying critical nucleation requirements under lower bulk supersaturation conditions. However, when the precipitant concentration increased to 1.5 M, the system entered a high-supersaturation spontaneous burst-nucleation region, and all systems exhibited coexistence of amorphous precipitates and small microcrystals (Figure 3D). These results indicate that the primary advantage of SNPs as nucleants lies in expanding the "low-supersaturation" crystallization window rather than suppressing disorder precipitation under highly supersaturated conditions.

3.4. Evidence for SNP–HEWL Interfacial Adsorption and Local Microenvironmental Perturbation

To further investigate the possible solid–liquid interfacial interactions involved in SNP-induced nucleation, systematic characterization of interfacial interactions was performed (Figure 4). Zeta potential analysis showed that the surface potentials of the 80, 120, and

200 nm SNPs in pH 4.6 buffer were −0.86, −3.29, and −13.2 mV, respectively, indicating that SNPs were negatively charged overall, whereas HEWL carried a net positive charge under these conditions. Therefore, charge complementarity may contribute to the interfacial association between SNPs and HEWL, although electrostatic interactions are likely screened under the relatively high ionic strength of the crystallization solution, and hydrogen bonding and surface hydration may also be involved. The more negative surface potential of the 200 nm SNPs was consistent with their shorter induction time and stronger nucleation-promoting effect, although Zeta potential reflects only the average surface charge state in solution and cannot independently prove interfacial binding strength or nucleation ability.

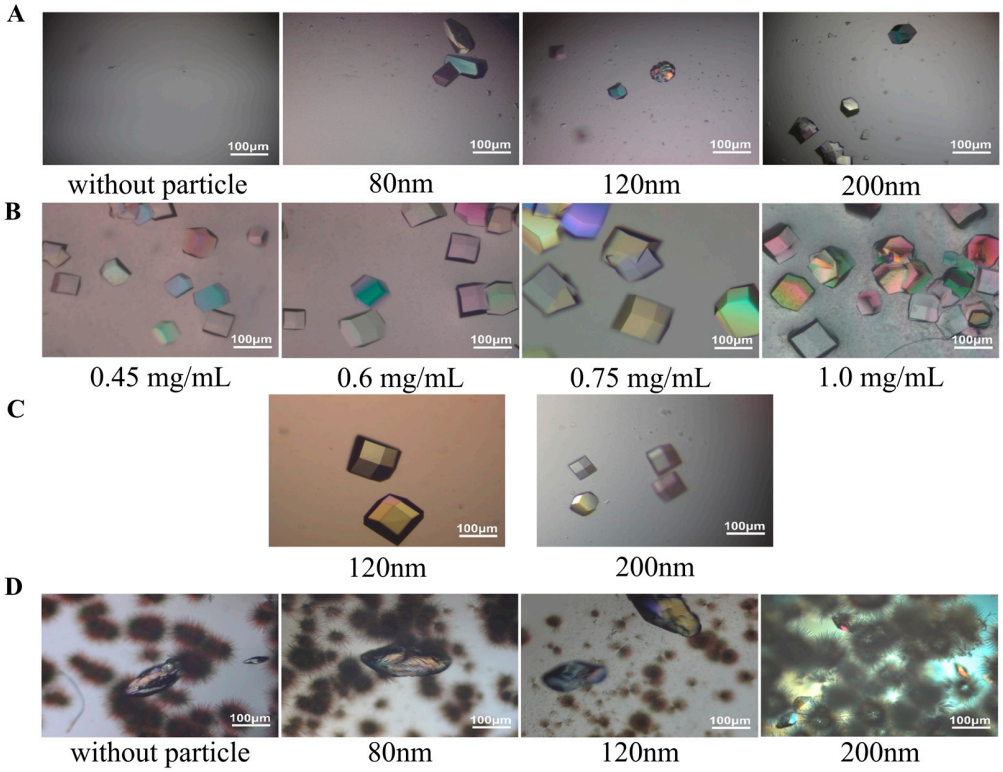

Figure 3. Effects of protein concentration, SNP dosage, and NaCl concentration on the crystallization behavior of HEWL. The colors observed in the optical micrographs result from optical imaging effects and have no specific scientific meaning. (**A**) Crystallization induction effects of SNPs with different particle sizes under low-protein-concentration conditions (15 mg/mL HEWL, 0.6 M NaCl; the total surface area of SNPs was maintained at 1.0×10^{16} $nm^2 \cdot mL^{-1}$). (**B**) Effects of different dosages of 200 nm SNPs on HEWL crystallization (30 $mg \cdot mL^{-1}$ HEWL, 0.6 M NaCl). (**C**) Crystallization induction behavior of SNPs with different particle sizes under 0.3 M NaCl conditions. (**D**) Crystal morphologies obtained in the presence of SNPs with different particle sizes under 1.5 M NaCl conditions.

Spectroscopic results further suggested interfacial interactions between SNPs and HEWL. After adding SNPs, a slight increase in UV absorption near 280 nm was observed, indicating possible changes in the microenvironment surrounding aromatic residues, although the magnitude of this change was relatively small. Fluorescence spectra showed significant quenching of intrinsic HEWL fluorescence, and the quenching effect became stronger with increasing SNP size, suggesting that the microenvironment surrounding Trp/Tyr residues was affected by SNP adsorption. Combined with the Zeta potential results, a reasonable interpretation is that HEWL molecules adsorbed onto SNP surfaces, resulting in local microenvironmental changes.

Slight shifts in the amide I and amide II bands were observed in the FT-IR spectra, suggesting that interactions between SNPs and HEWL may involve hydrogen bonding,

side-chain interactions, or local backbone vibrational changes. CD spectra showed that the far-UV spectral profiles of HEWL, HEWL + 80 nm, HEWL + 120 nm, and HEWL + 200 nm remained generally similar. Positive peaks near 190–195 nm and negative peaks near 205–210 nm were still present, and no obvious new peaks appeared in the 220–240 nm region, indicating that the overall folding framework of HEWL remained preserved after the addition of SNPs. Combined with the Zeta potential, UV-Vis, fluorescence, and FT-IR results, these findings suggest that interfacial interactions occurred between SNPs and HEWL without significantly disrupting the major secondary-structure characteristics of HEWL.

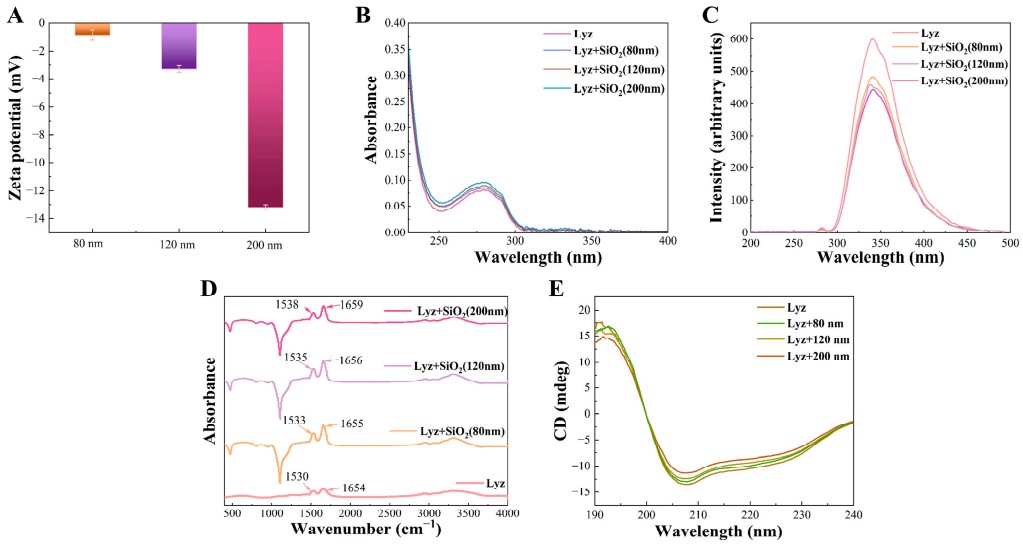

Figure 4. Spectroscopic and Zeta potential characterization of the interfacial interactions between SNPs and HEWL. (**A**) Zeta potentials of SNPs with different particle sizes. (**B**) UV-Vis absorption spectra of HEWL after interaction with SNPs. (**C**) Fluorescence quenching spectra of HEWL. (**D**) FT-IR spectra. (**E**) CD spectra.

3.5. Dynamic Analysis of Prenucleation Aggregate Formation

According to the two-step nucleation theory, protein crystallization in some systems may involve protein enrichment or prenucleation aggregate formation before stable nucleus formation. Therefore, DLS was used to monitor changes in the apparent hydrodynamic size of particles or composite aggregates in solution before visible crystal formation to evaluate the influence of SNPs on prenucleation aggregation behavior (Figure 5A,B). The particle-free control group exhibited slow hydrodynamic-size growth, suggesting that HEWL molecules gradually formed larger spontaneous aggregates. After introducing SNPs, scattering signals with larger hydrodynamic diameters appeared, indicating that HEWL may adsorb onto SNP surfaces and form protein–particle composite aggregates. The apparent size evolution trends of aggregates after adding different total surface areas of 200 nm SNPs (Figure 5C) further indicated that, within a certain range, the total surface area of SNPs strongly promoted the increase in aggregate hydrodynamic size.

Kinetic calculations (Figure 5D) showed that the apparent aggregation rate of the control group was 20.7 nm/min, whereas the rates for the 80, 120, and 200 nm SNP groups were 25.3, 400.0, and 86.8 nm·min^{-1}, respectively. The 200 nm SNP group exhibited the highest apparent aggregation rate, suggesting that larger SNPs may more effectively promote local HEWL enrichment and protein–particle aggregate formation at the solid–liquid interface. This trend was consistent with the shorter crystallization induction time observed in this system and supports the conclusion that SNPs mainly affect prenucleation processes.

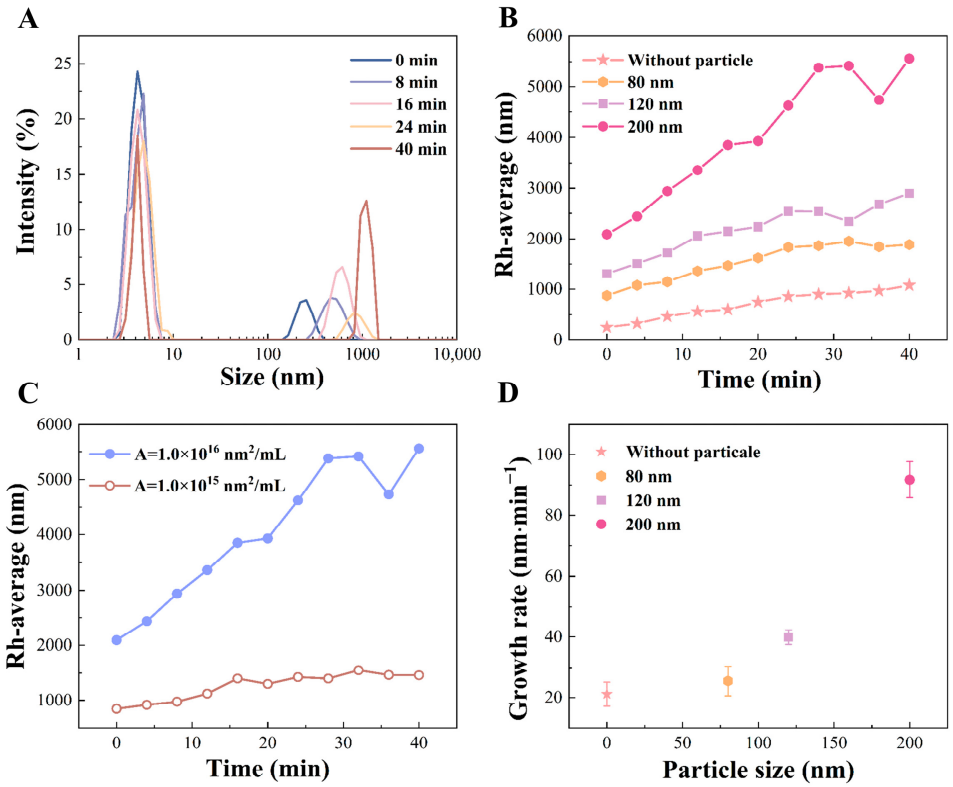

Figure 5. DLS kinetic characterization of prenucleation aggregate formation in the HEWL crystallization system. (**A**) Light scattering intensity distribution of the particle-free system. (**B**) Evolution curves of the apparent average hydrodynamic size after the addition of SNPs with different particle sizes. (**C**) Evolution curves of the apparent average hydrodynamic size after the addition of 200 nm SNPs with different total surface areas. (**D**) Comparison of apparent aggregation rates after the addition of SNPs with different particle sizes.

3.6. Subsequent Growth Dynamics of Visible Crystals

To decouple the respective impacts of SNPs on nucleation and crystal-growth stages, visible single crystals were tracked using polarized optical microscopy (Figure 6). Image analysis showed that the linear growth kinetics of characteristic crystal facets in the particle-free control group was 2.7 nm·s^{-1}, whereas the growth rate in the presence of 200 nm SNPs was 2.8 nm·s^{-1}. The nearly identical growth rates indicate that, once crystals reached optically visible sizes, 200 nm SNPs did not measurably affect subsequent linear crystal growth. Therefore, SNPs are unlikely to regulate HEWL crystallization by accelerating later crystal-face growth. These results suggest that the primary role of SNPs in HEWL crystallization is more likely associated with prenucleation aggregation and nucleus formation. Subsequent crystal growth may mainly depend on local supersaturation, solute diffusion, ordered incorporation of protein monomers into the crystalline lattice, and competition among neighboring crystals.

3.7. Molecular-Level Mechanism Investigation

To further investigate the possible molecular basis of SNP–HEWL interfacial interactions, molecular docking and molecular dynamics simulations were performed (Figure 7). The calculation results showed that SNP model clusters may bind to local charged or polar regions on the HEWL surface, with a minimum binding free energy of approximately −2.27 kcal·mol^{-1}, suggesting the existence of weak noncovalent interactions between SNPs and HEWL.

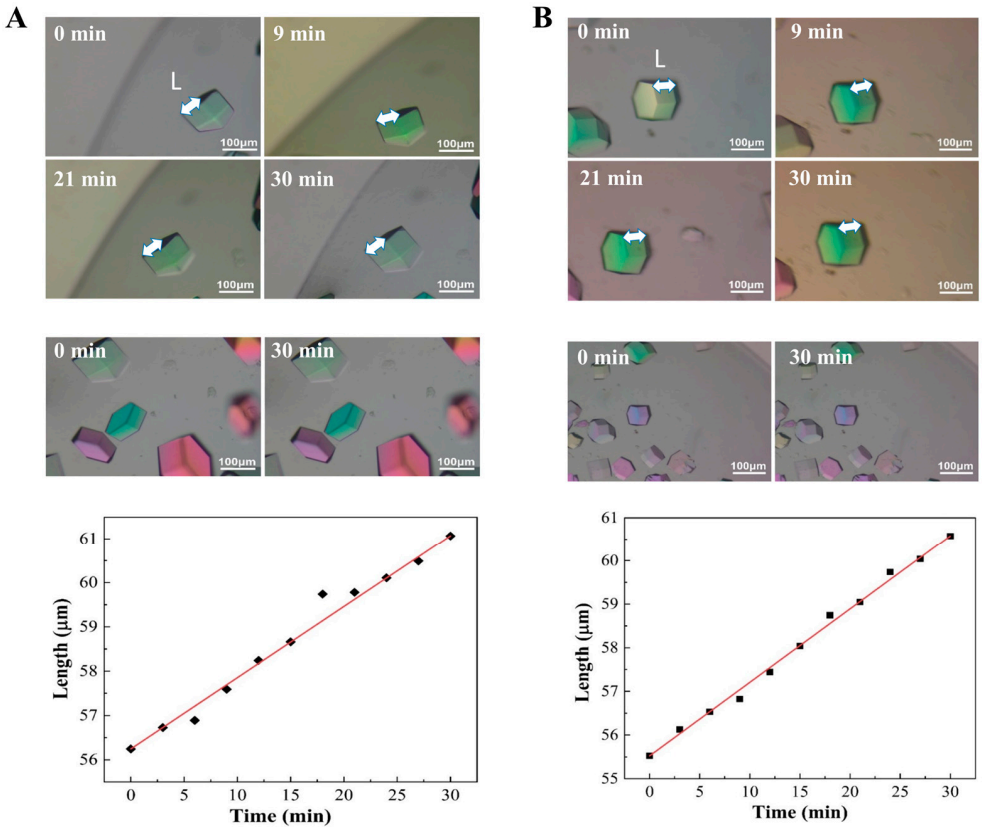

Figure 6. Subsequent growth process of HEWL crystals observed by polarized optical microscopy (upper panel: crystal images recorded at different time intervals within 30 min; lower panel: evolution of characteristic crystal edge length with time). (**A**) Particle-free control group without SNPs; (**B**) 200 nm SNP-containing system. The different colors observed in the crystal images arise from optical birefringence under polarized light and do not indicate differences in crystal composition or crystal form. The white double-headed arrows indicate the characteristic crystal dimension (*L*) used for growth analysis. Black diamonds represent the experimentally measured crystal lengths, and the red lines are linear fitting curves.

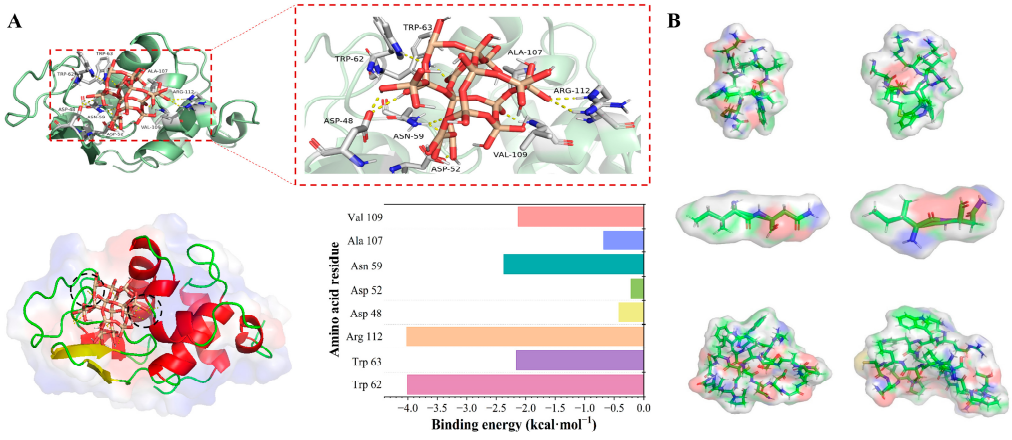

Figure 7. Possible mechanism supported by molecular docking and molecular dynamics simulations. (**A**) Possible binding conformations and key interacting residues between SNPs and HEWL. (**B**) Local surface topological changes before and after MD simulation. The simulation results provide a molecular-level interpretation of the proposed mechanism but do not constitute definitive proof of the nucleation mechanism.

Interaction analysis indicated that polar residues such as Arg112, Asp48, and Asp52 may participate in electrostatic interactions or hydrogen bonding, while residues near

Trp62, Trp63, and Ala107 may also contribute hydrophobic contacts, collectively stabilizing the SNP–HEWL interface. Notably, Trp62 and Trp63 were located near the predicted binding region, which was consistent with the fluorescence quenching behavior observed experimentally and may provide a possible explanation for changes in the aromatic residue microenvironment. MD simulations further showed that the SNP–HEWL complex maintained interfacial contact during the simulation process, providing auxiliary support for the interaction modes predicted by docking. The residues identified by docking should be interpreted as possible adsorption-related residues in the SNP–HEWL model, not as residues defining the final crystal packing contacts. SNPs mainly promote prenucleation precursors and local enrichment. Even at the SNP–precursor interface, the SNP only affects the first-layer arrangement; subsequent packing is governed by HEWL–HEWL interactions. Thus, overlap with packing residues does not imply templating. Docking and MD results provide qualitative support for interfacial adsorption, not crystal-packing control.

4. Conclusions

This study investigated the influence of 80, 120, and 200 nm SNPs on heterogeneous nucleation of HEWL. The results showed that all SNPs shortened the induction time of HEWL crystallization, with the 200 nm SNP group exhibiting the shortest induction time, whereas the 80 nm SNP group produced the largest crystal size at the fixed observation time of 72 h, suggesting that nucleation rate and crystal size within a fixed observation period do not exhibit a simple monotonic correlation. Low-protein-concentration and low-NaCl-concentration experiments further demonstrated that SNPs promoted HEWL nucleation under conditions with weak spontaneous nucleation. Zeta potential, UV-Vis, fluorescence, and FT-IR results supported the existence of interfacial interactions between SNPs and HEWL, while CD spectra indicated that the overall folding framework of HEWL remained preserved. DLS and microscopic observations further suggested that SNPs mainly influenced prenucleation protein–particle aggregate formation, whereas no measurable effect on subsequent visible crystal growth was detected. Overall, these results support a prenucleation-stage regulatory role of SNPs in HEWL crystallization, and their interfacial stabilization effects may involve electrostatic interactions, hydrogen bonding, and hydrophobic contacts. Although HEWL was used as a model, the SNP-assisted nucleation may extend to other net-positively charged proteins with exposed polar/charged patches that interact with negatively charged/hydrated silica. This applicability is conditional, not universal, as protein pI, surface properties, conformational stability, and solution conditions strongly influence the behavior. For acidic proteins, unmodified SNPs may be unfavorable without surface modification.

Supplementary Materials: The following supporting information can be downloaded at: https://www.mdpi.com/article/10.3390/cryst16070441/s1, Figure S1: The building of silica model for molecular docking: (a) crystal structure of silica, (b) amorphous silica, (c) spherical silica particles with unsaturated bonds, (d) spherical silica particles terminated by surface atoms; Figure S2: Processing of receptor protein model for molecular docking: (a) crystal structure of HEWL downloaded from PDB database, (b) HEWL structure after removing water molecules, (c) HEWL structure after hydrogenation; Figure S3: Visual representations of the helical structure and 10 Å silica spherical clusters before and after MD simulations: (a) SEG 1; (b) SEG 2; (c) SEG 3. Surface topological structures of the 10 Å silica spherical clusters before and after MD simulations: (d) SEG 1; (e) SEG 2; (f) SEG 3; Table S1: Summary of HEWL crystallization conditions; Table S2: Effect of precipitant concentration on HEWL crystallization in the absence and presence of silica nanoparticles. References [24–35,39,40] are cited in the supplementary materials.

Author Contributions: Conceptualization, X.C.; methodology, X.C.; software, X.C.; validation, Q.C.; formal analysis, X.Z.; investigation, Q.C. and X.C.; resources, X.Z.; data curation, Q.C. and X.C.;

writing—original draft preparation, Q.C.; writing—review and editing, Q.C.; visualization, X.C. All authors have read and agreed to the published version of the manuscript.

Funding: This work was financially supported by the Natural Science Foundation of Shanghai Municipality (No. 23ZR1417100).

Institutional Review Board Statement: Not applicable.

Data Availability Statement: The data presented in this study are available upon request from the corresponding author.

Acknowledgments: The authors would like to thank Yizhen Yan for his valuable discussions and insightful suggestions during the preparation and revision of this manuscript. His comments greatly contributed to improving the scientific interpretation and presentation of this work. During the preparation of this manuscript, the author Qihang Chen used ChatGPT (GPT-5.5 Thinking, OpenAI, 2026) only for the purposes of editing English writing to improve readability. The authors have reviewed and edited the output and take full responsibility for the content of this publication.

Conflicts of Interest: The authors declare no conflicts of interest.

References

1. Cole, J.M. Single-crystal X-ray diffraction studies of photo-induced molecular species. *Chem. Soc. Rev.* **2004**, *33*, 501–513. [CrossRef] [PubMed]
2. Margolin, A.L.; Navia, M.A. Protein crystals as novel catalytic materials. *Angew. Chem. Int. Ed.* **2001**, *40*, 2204–2222. [CrossRef]
3. Ko, T.-P.; Wang, Y.-C.; Yang, C.-S.; Hou, M.-H.; Chen, C.-J.; Chiu, Y.-F.; Chen, Y. Crystal structure and functional implication of bacterial STING. *Nat. Commun.* **2022**, *13*, 26. [CrossRef] [PubMed]
4. Samanta, D.; Zhou, W.; Ebrahimi, S.B.; Petrosko, S.H.; Mirkin, C.A. Programmable matter: The nanoparticle atom and DNA bond. *Adv. Mater.* **2022**, *34*, 2107875. [CrossRef]
5. Nicolas, W.J.; Gillman, C.; Weaver, S.J.; Clabbers, M.T.; Shiriaeva, A.; Her, A.S.; Martynowycz, M.W.; Gonen, T. Comprehensive microcrystal electron diffraction sample preparation for cryo-EM. *Nat. Protoc.* **2025**, *20*, 1275–1309. [PubMed]
6. Terwilliger, T.C.; Liebschner, D.; Croll, T.I.; Williams, C.J.; McCoy, A.J.; Poon, B.K.; Afonine, P.V.; Oeffner, R.D.; Richardson, J.S.; Read, R.J. AlphaFold predictions are valuable hypotheses and accelerate but do not replace experimental structure determination. *Nat. Methods* **2024**, *21*, 110–116. [PubMed]
7. Park, K.; Yoo, Y.; Jeon, H.; Choi, K.; Kim, H.; Kwon, E.; Lim, H.-H.; Kim, D.Y.; No, K.T. High-resolution cryo-EM structures of small protein–ligand complexes near the theoretical size limit. *Nat. Commun.* **2026**, *17*, 5188. [CrossRef] [PubMed]
8. Lu, W.; Zhang, J.; Huang, W.; Zhang, Z.; Jia, X.; Wang, Z.; Shi, L.; Li, C.; Wolynes, P.G.; Zheng, S. DynamicBind: Predicting ligand-specific protein-ligand complex structure with a deep equivariant generative model. *Nat. Commun.* **2024**, *15*, 1071. [CrossRef] [PubMed]
9. Zhang, Z.; Yang, X.; Zhao, Y.; Ye, F.; Shang, L. Liquid crystal materials for biomedical applications. *Adv. Mater.* **2023**, *35*, 2300220. [CrossRef]
10. Li, Z.; Wang, S.; Nattermann, U.; Bera, A.K.; Borst, A.J.; Yaman, M.Y.; Bick, M.J.; Yang, E.C.; Sheffler, W.; Lee, B. Accurate computational design of three-dimensional protein crystals. *Nat. Mater.* **2023**, *22*, 1556–1563. [CrossRef] [PubMed]
11. Li, J.; Deepak, F.L. In situ kinetic observations on crystal nucleation and growth. *Chem. Rev.* **2022**, *122*, 16911–16982. [CrossRef] [PubMed]
12. Aharoni, A. Theoretical search for domain nucleation. *Rev. Mod. Phys.* **1962**, *34*, 227. [CrossRef]
13. Erdemir, D.; Lee, A.Y.; Myerson, A.S. Nucleation of crystals from solution: Classical and two-step models. *Acc. Chem. Res.* **2009**, *42*, 621–629. [CrossRef] [PubMed]
14. Saridakis, E.; Chayen, N.E. Towards a 'universal'nucleant for protein crystallization. *Trends Biotechnol.* **2009**, *27*, 99–106. [CrossRef] [PubMed]
15. Binsbergen, F. Heterogeneous nucleation of crystallization. *Prog. Solid State Chem.* **1973**, *8*, 189–238. [CrossRef]
16. Chayen, N.; Saridakis, E.; El-Bahar, R.; Nemirovsky, Y. Porous silicon: An effective nucleation-inducing material for protein crystallization. *J. Mol. Biol.* **2001**, *312*, 591–595. [CrossRef] [PubMed]
17. Kertis, F.; Khurshid, S.; Okman, O.; Kysar, J.; Govada, L.; Chayen, N.; Erlebacher, J. Heterogeneous nucleation of protein crystals using nanoporous gold nucleants. *J. Mater. Chem.* **2012**, *22*, 21928–21934. [CrossRef]
18. Nanev, C.N.; Saridakis, E.; Chayen, N.E. Nucleation of protein crystals in pores and their growth. *Biophys. Rev.* **2025**, *17*, 935–946. [CrossRef] [PubMed]

19. Chen, W.; Park, S.J.; Kong, F.; Li, X.; Yang, H.; Heng, J.Y. High protein-loading silica template for heterogeneous protein crystallization. *Cryst. Growth Des.* **2019**, *20*, 866–873. [CrossRef]
20. Janjua, T.I.; Cao, Y.; Kleitz, F.; Linden, M.; Yu, C.; Popat, A. Silica nanoparticles: A review of their safety and current strategies to overcome biological barriers. *Adv. Drug Deliv. Rev.* **2023**, *203*, 115115. [CrossRef] [PubMed]
21. Molkova, E.A.; Pustovoy, V.I.; Stepanova, E.V.; Gorudko, I.V.; Astashev, M.E.; Simakin, A.V.; Sarimov, R.M.; Gudkov, S.V. PH-dependent HEWL-AuNPs interactions: Optical study. *Molecules* **2023**, *29*, 82. [CrossRef] [PubMed]
22. Zhang, Y.; Jiang, X.; Wu, X.; Wang, X.; Huang, F.; Li, K.; Zheng, G.; Lu, S.; Ma, Y.; Zhou, Y. Silica Nanoparticles-Induced Lysozyme Crystallization: Effects of Particle Sizes. *Crystals* **2022**, *12*, 1623. [CrossRef]
23. Brunauer, S.; Emmett, P.H.; Teller, E. Adsorption of gases in multimolecular layers. *J. Am. Chem. Soc.* **1938**, *60*, 309–319. [CrossRef]
24. Osterrieth, J.W.; Rampersad, J.; Madden, D.; Rampal, N.; Skoric, L.; Connolly, B.; Allendorf, M.D.; Stavila, V.; Snider, J.L.; Ameloot, R. How reproducible are surface areas calculated from the BET equation? *Adv. Mater.* **2022**, *34*, 2201502. [CrossRef]
25. Triantafyllidis, K.S.; Pinnavaia, T.J.; Iosifidis, A.; Pomonis, P.J. Specific surface area and I-point evidence for microporosity in nanostructured MSU-S aluminosilicates assembled from zeolite seeds. *J. Mater. Chem.* **2007**, *17*, 3630–3638. [CrossRef]
26. Takeda, Y.; Mafuné, F. Self-assembly of positively charged platinum nanoparticles in lysozyme crystal. *Chem. Phys. Lett.* **2014**, *604*, 110–115. [CrossRef]
27. Govada, L.; Leese, H.S.; Saridakis, E.; Kassen, S.; Chain, B.; Khurshid, S.; Menzel, R.; Hu, S.; Shaffer, M.S.; Chayen, N.E. Exploring carbon nanomaterial diversity for nucleation of protein crystals. *Sci. Rep.* **2016**, *6*, 20053. [CrossRef] [PubMed]
28. Xing, Y.; Hu, Y.; Jiang, L.; Gao, Z.; Chen, Z.; Chen, Z.; Ren, X. Zwitterion-immobilized imprinted polymers for promoting the crystallization of proteins. *Cryst. Growth Des.* **2015**, *15*, 4932–4937. [CrossRef]
29. Liu, Y.-M.; Li, H.-S.; Wu, Z.-Q.; Chen, R.-Q.; Lu, Q.-Q.; Guo, Y.-Z.; Zhang, C.-Y.; Yin, D.-C. Sensitivity of lysozyme crystallization to temperature variation. *CrystEngComm* **2016**, *18*, 1609–1617. [CrossRef]
30. Tanaka, S.; Ito, K.; Hayakawa, R.; Ataka, M. Size and number density of precrystalline aggregates in lysozyme crystallization process. *J. Chem. Phys.* **1999**, *111*, 10330–10337. [CrossRef]
31. Roberts, M.M.; Heng, J.Y.; Williams, D.R. Protein crystallization by forced flow through glass capillaries: Enhanced lysozyme crystal growth. *Cryst. Growth Des.* **2010**, *10*, 1074–1083. [CrossRef]
32. Longo, M.; Heigl, R.; Schrader, T.E. Real-time investigation of Lysozyme crystallization kinetics: A neutron diffraction study. *J. Cryst. Growth* **2021**, *576*, 126362. [CrossRef]
33. Yu, X.; Tian, N.; Huang, F.; Huang, X.; Liu, C.; Gao, S.; Yang, Z.; Wu, Y. Evaluating the role of ionic liquids (ILs) in the crystallization of lysozyme. *J. Mol. Liq.* **2019**, *296*, 112018. [CrossRef]
34. Gully, B.S.; Zou, J.; Cadby, G.; Passon, D.M.; Iyer, K.S.; Bond, C.S. Colloidal graphenes as heterogeneous additives to enhance protein crystal yield. *Nanoscale* **2012**, *4*, 5321–5324. [CrossRef] [PubMed]
35. Tang, L.; Huang, Y.; Liu, D.; Li, J.; Mao, K.; Liu, L.; Cheng, Z.; Gong, W.; Hu, J.; He, J. Effects of the silanized mica surface on protein crystallization. *Acta Crystallogr. Sect. D Biol. Crystallogr.* **2005**, *61*, 53–59.
36. Liu, Y.; Wang, X.; Ching, C.B. Toward further understanding of lysozyme crystallization: Phase diagram, protein− protein interaction, nucleation kinetics, and growth kinetics. *Cryst. Growth Des.* **2010**, *10*, 548–558. [CrossRef]
37. Lin, Z.; Tian, W.; Su, Y.; Yadav, V.K.; Yang, H. Positive and negative effects of graphite flake and monolayer graphene oxide templates on protein crystallization. *Particuology* **2023**, *79*, 27–34. [CrossRef]
38. Yan, Y.; Wang, J.; Lu, X.; Yuan, W.; Zhang, X. Nucleation-Supersaturation Dual-Drive Crystallization Strategy Enables Efficient Protein Crystallization. *Small* **2024**, *20*, 2307924. [CrossRef]
39. Zhang, Y.; Wang, Y.; Li, Y.; Zhang, Z. The mechanical properties of poly (urea-formaldehyde) incorporated with nano-SiO_2 by molecular dynamics simulation. *Polymers* **2019**, *11*, 1447. [CrossRef] [PubMed]
40. Wu, Y.; Zhang, H.; Wang, Y. Conformational and functional changes of bovine serum albumin induced by TiO_2 nanoparticles binding. *J. Mol. Liq.* **2017**, *243*, 358–368. [CrossRef]
41. Liu, H.; Zhao, Y.; Sun, J. Heterogeneous nucleation in protein crystallization. *Biomimetics* **2023**, *8*, 68. [CrossRef] [PubMed]
42. Artusio, F.; Gavira, J.A.; Pisano, R. Self-assembled monolayers as a tool to investigate the effect of surface chemistry on protein nucleation. *Cryst. Growth Des.* **2023**, *23*, 3195–3201. [CrossRef] [PubMed]